Available online at www.sciencedirect.com

ScienceDirect

Procedia Structural Integrity 35 (2022) 168–172

Structural Integrity Procedia

www.elsevier.com/locate/procedia

2nd International Workshop on Plasticity, Damage and Fracture of Engineering Materials

Deformation of AlSi10Mg parts manufactured by Laser Powder Bed Fusion: *In-situ* measurements incorporating X-ray micro computed tomography and a micro testing stage

Joachim Koelblin[a]*, James C. Hastie[a], Mehmet E. Kartal[a], Amir Siddiq[a], Moataz M. Attallah[b]

[a]*University of Aberdeen, School of Engineering, Fraser Noble Building, Kings College, Old Aberdeen, Aberdeen AB24 3UE, United Kingdom*
[b]*University of Birmingham, School of Metallurgy and Materials, Edgbaston, Birmingham B15 2TT, United Kingdom*

Abstract

The latest advances in optimising the process parameters of laser powder bed fusion (LPBF) result in high densification part. Nonetheless, slight variations of those parameters or the use of recycled powder leads to sub-optimal parts, containing more defects. AlSi10Mg samples were produced by LPBF using recycled powder to study the effect of process-induced defects and their evolution under increased tensile load. This is achieved by employing an *in-situ* micro testing stage combined with high-resolution X-ray micro computed tomography (XμCT). This combined approach provides three-dimensional (3D) images at multiple load increments. These images are then used to calculate the internal strains between defects in subsequent loading stages and are reported in this work.

Keywords: Laser powder bed fusion; Selective laser melting; Tensile testing; Internal porosity; *in-situ* X-ray computed tomography; Digital image correlation

1. Introduction

Over the last decade, many industrial sectors have been increasingly adopting Laser Powder Bed Fusion technology, also referred to as Selective Laser Melting, owing to its capability to produce near-net shape complex components from a CAD model and hence offering robust design flexibility without the constraints of conventional manufacturing methods that require a series of manufacturing processes, more material consumption, higher cost and energy, Gibson et al. (2010), Brandl et al. (2012), DebRoy et al. (2018).

Despite offering numerous benefits, LPBF in a production environment can lead to sub-optimal parts (i.e., often refers to a part with densification less than 98.5%) due to constraints such as machine capabilities, the use of recycled powder and time constraints, Tradowsky et al. (2016). Even with the state-of-the-art advances in LPBF, parts with 99.9% densification still include defects that result in scattering in the mechanical performance of the parts, Hastie et al. (2020). The driving force behind such inconsistency is due to randomly distributed defects including gas pores, voids or cracks which are formed during solidification. As each defect is different in size, shape and location, so is its contribution to damage progressions, Awd et al. (2017).

* Corresponding author.
E-mail address: j.koelblin.18@abdn.ac.uk (J. Koelblin).

10.1016/j.prostr.2021.12.061

In the previous study of Hastie et al. (2021), the evolution of internal defects under increasing tensile load was investigated, thus focussing on the change in pore shape, damage propagation and pore coalescence. In the present study, the Digital Image Correlation (DIC) methodology by which internal strain is calculated from the obtained XμCT images is described.
Thus, analysing the strain evolution in the vicinity of defects during tensile testing.

Nomenclature

A-1	As-built sample 1
A-2	As-built sample 2
DIC	Digital Image Correlation
HIP	Hot Isostatic Pressing
HT6	Sample that has undergone hot isostatic pressing and subsequent T6 heat treatment
LPBF	Laser Powder Bed Fusion
T6	T6 heat treatment
XμCT	X-ray micro computed tomography

2. Experimental procedure and methodology

LPBF was the manufacturing method used to produce miniature tensile testing specimens from recycled AlSi10Mg powder, leading to sub-optimal densification. To acquire 3D images of the defects and their evolution under different stages of increasing tensile loading, a combination of high-resolution XμCT and an *in-situ* micro-testing stage was utilised as described in Hastie et al. (2021). Samples in three different heat-treated conditions, namely as-built, HIPped and HIPped + T6, were tested *in-situ*. In their study, the elongation was measured at a crosshead of the tensile testing stage and hence it involves the combined effect of actual deformation and compliance of the machine. While such data gives an indication on the material behaviour, it does not allow for a detailed analysis of the microstructural effect on deformation. In order to eliminate machine compliance and measure net strain caused by deformation in this study, XμCT datasets of the same sample at subsequent loading increments were loaded into the Python 3.8 programming environment, using the DXchange package from De Carlo et al. (2014) and each 3-dimensional XμCT image is decomposed into a dataset containing a stack of 2-dimensional images as illustrated in Fig. 1a, where each plane depicts the morphological cross-section of the sample normal to the loading direction. The data contained in one such plane is depicted in Fig. 1b. Like many other visualization methods of datasets it is plotted using the Matplotlib package from Hunter (2007). To eliminate the variations between images induced by noise, differences in illumination or contrast, threshold values are imposed to each dataset such that only the morphology of the defects remains as bright features, Fig. 1c. Furthermore, the datasets are rearranged according to the applied load direction. While each of these planes contains the cross-sectional morphology of the defects at its load increment, it is not guaranteed that the same plane in the subsequent loading stage holds the same features (due to damage accumulation) with an offset only in the loading direction. Thus, multiple planes of the initial datasets are selected and correlated to the planes of the subsequent loading stage using SciPy from Virtanen et al. (2020) and NumPy from Harris et al. (2020) to find pairs of matching planes.

Using those matching planes, the defects from the initial deformation stage are extracted by selecting enclosing edges using SciPy, and are then correlated to the paired image, individually. By comparing the distances between the defects in the initial stage and the subsequent loading stage, the strains in-between the defects are calculated. Based on the correlation indices and monitoring the resulting correlation, lower boundaries which only consider defects above a certain size and correlation coefficient are applied. By incrementally adapting those boundaries and analysing the resulting correlation, the boundaries were set at defects with at least one edge greater than 20 pixels and a correlation value of more than 60%.

Following this methodology, results in separate strain fields for each of the selected planes, as shown in Fig. 2a. To eliminate outliers the final strain increment is calculated by taking the median of all calculated strain values and written to a text file alongside with the threshold settings.

3. Results and discussion

The *in-situ* nominal stress vs. extension curve, shown in Fig. 2b, was measured based on the crosshead displacement of the employed tensile testing stage and hence involves the combined effect of deformation and compliance of the machine. Therefore, actual deformation on the sample is significantly covered by the compliance of machine. As can be seen in Fig. 2b, drops along the load curve occur at the targeted load stages where the XμCT scans were taken at a constant extension level. Prior to each scan, the sample was held at the required extension for about an hour to minimise the effect of stress relaxation and ensure the image quality.

By utilizing the DIC algorithm described in Section 2, the strains in-between the load increments are calculated and combined to produce the nominal stress vs. strain plot shown in Fig. 2c. Unlike Fig. 2b, this figure clearly shows the transition from elastic to the plastic deformation of the sample. Nonetheless, compared to Fig. 2b the curve is coarser which is due to the number of scanned load increments. However, following the same approach a finer curve could be plotted, by increasing the number of scans,

using the same outlined approach. While Fig. 2b showed some offset in-between the two as-built samples, Fig. 2c shows that the tensile properties of both samples are comparable when machine compliance is removed from total elongation.

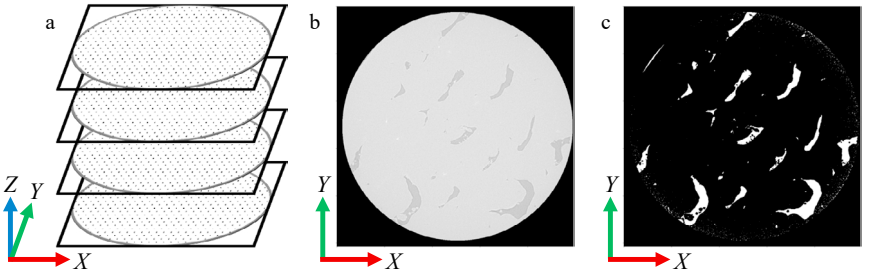

Fig. 1. (a) Example of sliced and stacked XµCT dataset where the slices are perpendicular/normal to the applied load direction; (b) Single slice extracted from the XµCT dataset without any post-processing; (c) Threshold slice showing the extracted defects in white and remainder in black.

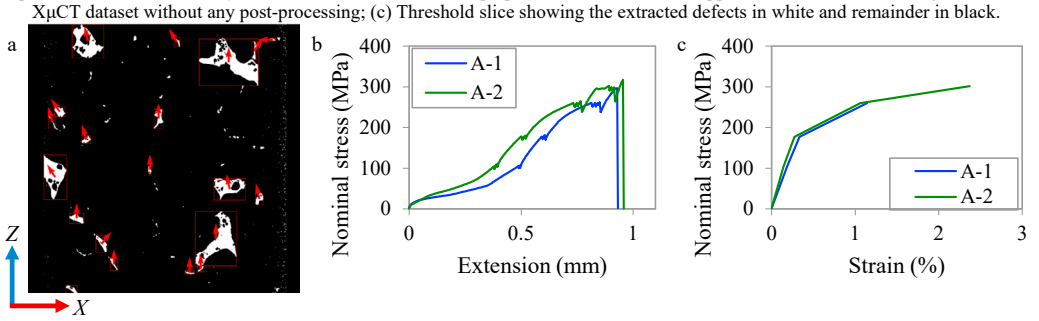

Fig. 2. (a) Cross-section which has been threshold and aligned with the load direction. Additional quivers indicate the calculated strain direction; (b) In-situ measurement of nominal stress vs. extension; (c) Nominal stress vs. strain calculated according to the outlined procedure.

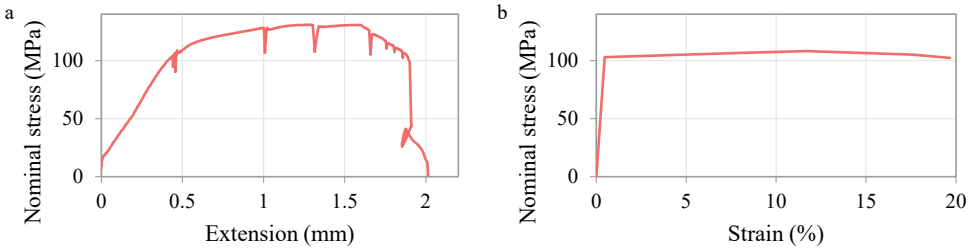

Fig. 3. (a) HIPped sample: *In-situ* measurement of nominal stress vs. extension; (b) HIPped sample: Nominal stress vs. strain calculated according to the outlined procedure.

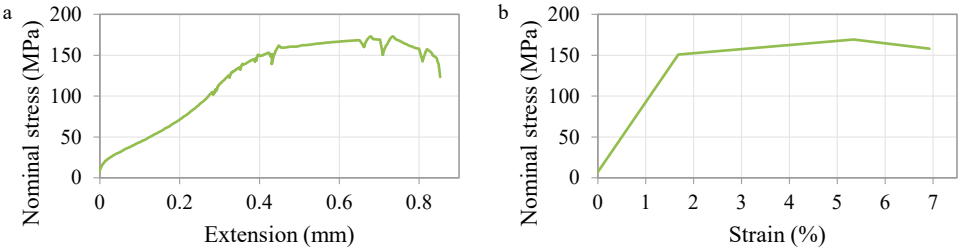

Fig. 4. (a) HIPped + T6 sample: In-situ measurement of nominal stress vs. extension; (b) HIPped + T6 sample: Nominal stress vs. strain calculated according to the outlined procedure.

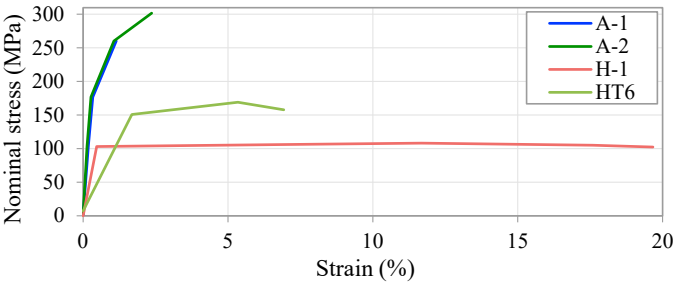

Fig. 5. Summary of all *in-situ* nominal stress vs. strain curves.

In comparison to the as-built condition, the nominal stress in the HIPped condition is significantly lower, Fig. 3a. However, as a result of DIC, Fig. 3b reveals that actual deformation of HIPped sample in comparison with the as-built condition increases by almost a factor of 10. It can also be observed that while the first load increment mainly caused an elastic material response, the subsequent loading caused plastic deformation without any significant hardening effect.

Applying a T6 solution treatment after HIPping slightly increases the amount of nominal stress, as shown in Fig. 4a. While the amount of extension of the HT6 sample is comparable to the as-built samples shown in Fig. 2b, the measured elongation after HIPping + T6, shown in Fig. 4b exceeds its as-built counterparts. However, the tensile strength of the as-built samples could not be reached.

As shown in Fig. 5, from all the tested material conditions the as-built condition exhibits the highest tensile strength, while the highest elongation is observed in the HIPped condition. Furthermore, the Young's modulus in this both conditions is comparable. On the other hand, the Young's modulus of the HT6 sample appears much lower. Such discrepancy is attributed to the first load increment in the HT6 condition where plastic deformation took place while the first load increment for all other samples mainly include elastic deformation. This highlights how susceptible the DIC approach is in terms of the load increments.

To assess the overall reliability of the calculated strain, the strain calculation was repeated for the as-built case at an additional section of the sample. While in an ideal sample the strains in different parts of the gauge section are constant, the natural variations of the microstructure in the scanned sample causes local fluctuations in the measured strains. Such fluctuations are also occurring in-between the two tested locations of both the as-built samples, as summarised in Table 1. The overall consistent strain values together with the tight variance shows that the outlined DIC approach produces reliable results.

Table 1. Strain increment at two locations per sample during multiple load increments

		Location 1		Location 2	
	Extension (mm)	Strain [%]	Variance	Strain [%]	Variance
As-built 1	0.49	0.169	0.0036	0.198	0.0093
	0.62	0.140	0.0023	0.159	0.0055
	0.84	0.945	0.0042	0.673	0.0063
As-built 2	0.39	0.121	0.0092	0.164	0.0296
	0.55	0.130	0.0038	0.130	0.0045
	0.75	0.802	0.0023	0.776	0.0063
	0.91	1.34	0.0058	1.27	0.0366

4. Conclusions

This study shows that the internal strain state of a material can be recovered based on the defects located within subsequent XμCT datasets. While previously the compliance of the tensile testing stage limited the accuracy, the presented method can be used for a more detailed analysis relating pores and deformation, also allowing to determine between elastic and plastic regimes if enough scans are available.

As this approach is dependent on the presence of defects within slices of the scanned sample, adapting the algorithm to include 3D correlation of defects could lead to an increased range of future applications.

Acknowledgements

The authors gratefully acknowledge the financial support of the Engineering and Physical Sciences Research Council (EPSRC) under grant reference EP/R021694/1, "3D *in-situ* based methodology for optimizing the mechanical performance of selective laser melted aluminium alloys".

References

Awd, M. et al., 2017. Comparison of Microstructure and Mechanical Properties of Scalmalloy(®) Produced by Selective Laser Melting and Laser Metal Deposition. Materials (Basel, Switzerland) 11 (1), 17.

Brandl, E., Heckenberger, U., Holzinger, V., Buchbinder, D., 2012. Additive manufactured AlSi10Mg samples using Selective Laser Melting (SLM): Microstructure, high cycle fatigue, and fracture behavior. Materials & Design 34 159–169.

De Carlo, F. et al., 2014. Scientific data exchange: a schema for HDF5-based storage of raw and analyzed data. Journal of Synchrotron Radiation 21 (6), 1224–1230.

DebRoy, T. et al., 2018. Additive manufacturing of metallic components – Process, structure and properties. Progress in Materials Science 92 112–224.

Gibson, I., Rosen, D. W., Stucker, B., 2010. Additive Manufacturing Technologies: Rapid Prototyping to Direct Digital Manufacturing. In *Springer* Springer US.

Harris, C. R. et al., 2020. Array programming with NumPy. Nature 585 (7825), 357–362.

Hastie, J. C., Kartal, M. E., Carter, L. N., Attallah, M. M., Mulvihill, D. M., 2020. Classifying shape of internal pores within AlSi10Mg alloy manufactured by

laser powder bed fusion using 3D X-ray micro computed tomography: Influence of processing parameters and heat treatment. Materials Characterization 163 (October 2019), 110225.

Hastie, J. C., Koelblin, J., Kartal, M. E., Attallah, M. M., Martinez, R., 2021. Evolution of internal pores within AlSi10Mg manufactured by laser powder bed fusion under tension: As-built and heat treated conditions. Materials and Design 204 109645.

Hunter, J. D., 2007. Matplotlib: A 2D Graphics Environment. Computing in Science & Engineering 9 (3), 90–95.

Tradowsky, U. et al., 2016. Selective laser melting of AlSi10Mg: Influence of post-processing on the microstructural and tensile properties development. Materials and Design 105 212–222.

Virtanen, P. et al., 2020. SciPy 1.0: fundamental algorithms for scientific computing in Python. Nature Methods 17 (3), 261–272.